JPhys Energy

PAPER • OPEN ACCESS

Li^+ concentration and morphological changes at the anode and cathode interphases inside solid-state lithium metal batteries

To cite this article: Chun Huang *et al* 2025 *J. Phys. Energy* **7** 025009

IOP Publishing J. Phys. Energy 7 (2025) 025009 https://doi.org/10.1088/2515-7655/adafda

Journal of Physics: Energy

OPEN ACCESS

RECEIVED
9 November 2024

REVISED
19 January 2025

ACCEPTED FOR PUBLICATION
29 January 2025

PUBLISHED
12 February 2025

PAPER

Li^+ concentration and morphological changes at the anode and cathode interphases inside solid-state lithium metal batteries

Chun Huang[1,2,3,*], **Matthew D Wilson**[4], **Ben Cline**[4], **Abeiram Sivarajah**[1], **Wiebe Stolp**[5], **Matthieu N Boone**[5], **Thomas Connolley**[6] and **Chu Lun Alex Leung**[3,7]

[1] Department of Materials, Imperial College London, London SW7 2AZ, United Kingdom
[2] The Faraday Institution, Didcot OX11 0RA, United Kingdom
[3] Research Complex at Harwell, Rutherford Appleton Laboratory, Didcot OX11 0FA, United Kingdom
[4] STFC-UKRI, Rutherford Appleton Laboratory, Didcot OX11 0QX, United Kingdom
[5] Radiation Physics, Department of Physics and Astronomy, Ghent University, Proeftuinstraat 86/N12, 9000 Gent, Belgium
[6] Diamond Light Source, Didcot OX11 0QX, United Kingdom
[7] Department of Mechanical Engineering, University College London, London WC1E 7JE, United Kingdom
[*] Author to whom any correspondence should be addressed.

E-mail: a.huang@imperial.ac.uk

Keywords: solid-state batteries, correlative imaging, lithium ion concentration, microstructure, x-ray Compton scattering, mass transport

Supplementary material for this article is available online

Abstract

Irregular Li heterostructure growth at the interphase between the solid electrolyte and anode reduces solid-state Li metal battery (SSLMB) performance, but the fundamental cause is still elusive. Measuring and imaging Li^+ ion diffusion *in operando* inside an SSLMB using a commercially standard cell configuration are extremely challenging because the ultra-light Li element exhibits a minute signal-to-noise ratio using most x-ray-related characterization methods, and the weak x-ray signals of Li^+ are buried by strong signals of other heavy transition metal elements in the cathode and battery enclosure. Here, we pioneer novel *operando* correlative imaging of coupling x-ray Compton scattering with computed tomography (XCS-CT), which is able to quantify the interplay between spatially resolved Li^+ ion diffusion kinetics and Li^0 metal structure growth at the interphases of both the anode and cathode sides inside a full-cell SSLMB using a solid polymer electrolyte (SPE) and commercially standard cell configuration during (dis)charging. We show a 61% increase in the efficiency of extracting Li^+ ions from the cathode $LiNi_{0.6}Mn_{0.2}Co_{0.2}O_2$ to the anode during charging at 0.1 C compared with at 1 C due to restricted Li^+ ion diffusion at the higher rate inside SSLMB. However, this led to the formation of a more irregular interfacial morphology, consisting not only of Li^0 dendrites, but also sub-surface pore formation at the anode/SPE interphase. We find that surprisingly, the irregular Li^0 structure initiation and growth are accelerated during the first Li stripping step, not the Li plating step, and the root cause is the onset imbalance of Li^+ ion diffusion and redox reactions between the anode and cathode. These insights highlight the benefits of asymmetric charging and discharging rates as a promising solution to improving SSLMB performance with SPEs. The *operando* correlative XCS-CT imaging technique has the potential to study the relationship between active ion concentrations and buried morphological changes for a variety of battery chemistries.

1. Introduction

Rechargeable batteries are a key technology in enabling net zero applications through reducing greenhouse gas emissions and the reliance on fossil fuels [1]. Li ion batteries (LIBs) have been ubiquitously used, while other battery chemistries have also attracted significant research interest [2, 3]. It is attractive to use a Li metal anode due to its significantly higher theoretical capacity (3860 mAh g^{-1}) compared to conventional graphite anodes (372 mAh g^{-1}) [4]. Solid-state Li metal batteries (SSLMBs) replace the traditional

combustible liquid electrolytes in LIBs with non-flammable solid-state electrolytes (SSEs), and hence, SSLMBs are potentially safer than LIBs and increase the theoretical energy density from ∼300 Wh kg^{-1} for LIBs to ∼500 Wh kg^{-1} through the use of the pure Li anode [5]. Solid electrolytes are mainly categorized into two types: one is solid inorganic electrolytes (SIEs) and the other is solid polymer electrolytes (SPEs). SIEs consist of crystalline or glassy materials, including sulfides, phosphates, or oxides [6]. They exhibit well-organized and rigid structures that facilitate ion diffusion. SPEs comprise polymers that are infused with ionic salts; they exhibit amorphous characteristics and mechanical flexibility, providing benefits in processability and high compatibility with a wide range of battery configuration designs [7]. This paper will focus on SPE-based SSLMBs.

The significant morphological changes of Li at the anode/SSE interphase are key factors restricting the performance of SSLMBs [8]. Li dendrite growth and Li structure penetration from the anode to the cathode cause safety hazards [9]. Slippage is a phenomenon that describes the capacity shift between the cathode and anode relative to their capacity alignment at the start of charging and discharging, and this phenomenon has been studied in liquid electrolyte batteries [10, 11]. Three-dimensional structures of high areal capacities have also been developed on the cathode side [12]. However, Li^+ ion concentration changes and morphology changes at the cathode and anode interphases within the same full-cell SSLMB have rarely been compared to unveil the onset of the imbalance between the cathode and anode behavior [13].

Li intrusion through an SSE of $Li_7La_3Zr_2O_{12}$ was observed using scanning electron microscopy *in operando* [14]. *Operando* optical interferometric scattering microscopy observed Li^+ ion dynamics at the nanoscale inside individual particles of a Li_xCoO_2 cathode [15] and $Nb_{14}W_3O_{44}$ anode [16]. Li whisker growth under elastic constraint was studied by atomic force microscopy combined with transmission electron microscopy [17]. Variable energy positron annihilation lifetime spectroscopy coupled with tip-enhanced Raman spectroscopy was used to assess $LiMn_2O_4$ cathode stability in aqueous electrolytes from the atomic to the micrometer scale [18]. Atom probe tomography was used to provide compositional mapping in 3D including Li [19]. However, these methods typically have a relatively small observation field-of-view of a few micrometers and are unable to observe Li structures at the buried interphases within commercially standard battery configurations.

To examine complete cells, x-ray computed tomography [20, 21], x-ray radiography [22], and neutron radiography were used to image Li propagation and crack growth in a Li_6PS_5Cl SSE [21], but these methods are based on the attenuation coefficients of different materials and cannot distinguish between Li^+ and Li^0 [23]. It is notoriously challenging to measure the ultra-light Li^+ directly using conventional x-rays because of the minute signal-to-noise-ratio that the ultra-light Li exhibits. X-ray near-edge absorption spectroscopy and x-ray absorption fine-structure spectroscopy are able to quantify chemical properties, such as oxidation states of elements, through characteristic edge spectra of the K, L, and M electron shells [24], but it is more sensitive toward heavy transition elements that have more electron shells, and has a low sensitivity toward quantifying Li, which has only three electrons and two electron orbitals. X-ray fluorescence (XRF) also cannot detect Li, and hence $LiAsF_6$ salt was deliberately added in the liquid electrolyte as a model system, and the signals of the element As were measured by XRF to infer Li concentration in the electrolyte [25]. Furthermore, it is challenging to use conventional XRD to measure amorphous materials (e.g. polymer electrolytes) [26]. Pair-distribution functions combined with modeling have been used to understand material local disorder, but it is challenging to perform *in situ* experiments using electrodes and battery configurations that represent commercially standard operations since other components such as binders and carbon black are needed for the battery electrochemical operation, which may interfere with the active material results [27]. Nuclear magnetic resonance is one of the few techniques that is able to directly study Li [28, 29], but it usually requires bespoke cell configurations [30]. Different electrochemical testing methods have been used to measure the changes in interfacial resistance and indirectly investigate the formation and annihilation of micropores at the anode/SSE interphase [8]. Nevertheless, showing the relationship between the Li^+ ion concentration and Li^0 morphology changes simultaneously using the same technique has not been fully explored.

Herein, we investigate a full-cell SSLMB containing a cathode of $LiNi_{0.6}Mn_{0.2}Co_{0.2}O_2$ (NMC622) active material, a Li metal anode, and a polyethylene oxide (PEO)-based SPE, housed in a commercially standard coin cell configuration using novel *operando* correlative imaging of x-ray Compton scattering and computed tomography (XCS-CT), which can shed new light on the interfacial behavior inside devices. XCS is x-ray inelastic scattering that measures the Li^+ ion concentration distributions by calculating the valence electron momentum of the electrode materials to amplify the ultra-light Li^+ signals, while CT shows the changes in Li^0 morphology at the buried interphase between the SPE membrane and the anode inside the SSLMB. We correlate spatially resolved Li chemical evolution and structural deviation at the interphases on both the anode and the cathode sides at different (dis)charge rates. We show that there were larger changes in Li^+ ion concentration at both interphases at a 0.1 C (dis)charge rate compared to 1 C due to restricted Li^+ ion

diffusion in the SSLMB at higher rates. The morphological changes at the anode/SPE interphase were more significant than those at the cathode/SPE interphase. Li dendrites grew from the anode toward the cathode during Li plating, but the growth direction was deflected by the SPE membrane. Irregular Li structures continued to grow during Li stripping due to an imbalance of Li^+ ion diffusion and redox reactivity between the anode and the cathode. Potential suitable strategies toward reducing irregular Li metal structures at the anode/SPE interphase include interfacial engineering, such as developing a polymer-inorganic solid electrolyte interphase, e.g. composite of poly(vinylsulfonyl fluoride-*ran*-2-vinyl-1,3-dioxolane)-graphene oxide nanosheet [31], adding hollow porous SiO_2 nanosphere fillers in the SPE to increase ionic conductivity and SPE mechanical strength [32], asymmetric charging and discharging protocols [33], and using a high-current discharge for 1–2 min to induce isolated Li to dissolve on one end and re-deposit on the other end to re-connect to the anode [34]. The *operando* correlative XCS-CT imaging technique can also be applied to other battery chemistries, such as Na batteries [2].

2. Method

2.1. Fabrication of SSLMB and electrochemical testing

PEO (molecular weight of 1000 000 g mol^{-1}) was mixed with lithium bis(trifluoromethanesulfonyl)imide (LiTFSI). The mixture was dissolved in the solvent acetonitrile ([PEO]:[Li^+] = 15:1) and constantly stirred at 60 °C for 24 h before being cast. The resulting polymer composite electrolyte membrane was dried at 40 °C for 24 h to evaporate acetonitrile and form SPE films of 30 μm in thickness. The ionic conductivity of the SPE membranes was evaluated through electrochemical impedance spectroscopy (EIS) in a symmetric cell configuration comprising an SPE membrane sandwiched between two spacers made of stainless steel at a frequency range of 10^5–0.1 Hz and an amplitude perturbation of 10 mV at 25 °C, 50 °C, and 80 °C. The ionic conductivity (σ) of SPE was estimated by equation (1) [35]:

$$\sigma = \frac{L}{R_s \times A} \tag{1}$$

where R_s is the intercept between the Nyquist plot and Z_{real}, A is the area, and L is the thickness of the SPE.

To prepare cathodes, NMC622 active material, carbon black particulates, and polyvinylidene fluoride binder of 90:5:5 wt.% were homogeneously mixed and dispersed in N-methyl pyrrolidine, coated on Al foils, and dried at 80 °C under a vacuum for 12 h. The average cathode mass loading and density were 19.3 mg cm^{-2} and 2.97 g cm^{-3}, respectively. The PEO-LiTFSI solution was drop cast onto the cathodes to form composite cathodes that were then dried at 60 °C for 12 h as previously reported in [36]. The Li anode, SPE membrane, and composite cathode were finally assembled into standard stainless steel coin cells (CR2032) inside a glovebox filled with Ar. Rate capability testing of *ex situ* (dis)charge of at different C rates, cycling stability at 0.2 C, and linear sweep voltammetry (LSV) at 0.5 mV s^{-1} scan rate of full-cell SSLMBs were performed at 60 °C using the testing protocols previously reported in [37]. EIS of the SSLMBs was performed at a frequency range of 10^5–0.1 Hz at the states of pristine, end of charge, and end of discharge of the first cycle at 60 °C.

2.2. *Operando* correlative XCS-CT imaging

A monochromatic x-ray beam of high energy (115 keV) was used at the beamline I12-JEEP (Joint Engineering, Environmental and Processing) at Diamond Light Source, UK. For CT, a box x-ray beam (25 × 5 mm^2) was used in order to scan the whole battery. A camera (PCO.Edge 5.5 sCMOS) with a scintillator using a 0.82× magnification lens was placed behind the battery sample to take x-ray transmission images. The CT scans consisted of 3600 projections of 360° using 9 ms exposure time per projection. For XCS imaging, the x-ray beam was changed into a sheet beam (25 × 0.25 mm^2) through x-ray beam-defining slits, and the *x*–*y* (horizontal) plane of the SSLMB was aligned parallel to the incident sheet beam. The scattered photons were collected at 90° to the x-ray beam above the battery sample through a 2D high-energy x-ray imaging technology (HEXITEC) detector made of CdZnTe [38]. XCS imaging was projected through a pinhole (0.2 mm in diameter) in a W plate (2 mm in thickness) at a distance ratio of 1:1 between the sheet beam position and the pinhole, and between the pinhole and the detector. The HEXITEC detector consisted of 80 × 80 pixel arrays and collected an energy-resolved x-ray spectrum per pixel at a spectral resolution of ∼800 eV. The HEXITEC detector obtained the energy spectra of all pixels along the horizontal plane simultaneously [39]. The vertical position of the battery sample was moved so that the sheet beam probed three different planes of the battery: region 1 contained the cathode, the SPE membrane, and a part of the anode; region 2 contained the SPE membrane and a part of the anode; and region 3 contained the anode only, as shown in figure 1, which also shows homogeneous contact among the anode, SPE membrane, and cathode in the pristine state.

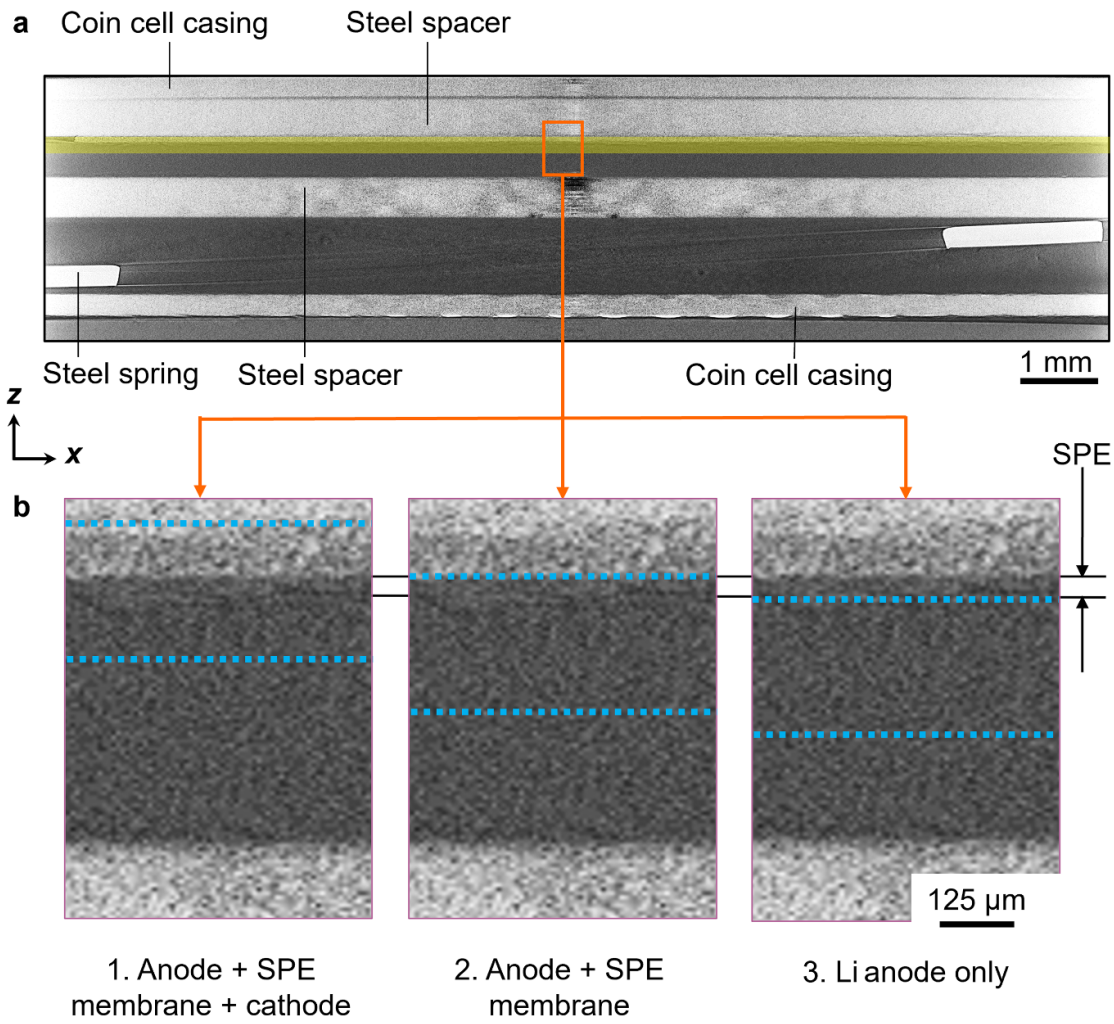

Figure 1. The reconstructed CT *x*–*z* slice shows the internal components of the pristine SSLMB coin cell. The false yellow color in (a) shows the regions of interest, and the blue dotted lines in (b) illustrate the three different vertical positions of the x-ray sheet beam probing the different planes of the coin cell during XCS imaging.

During the synchrotron XCS-CT experiment, the SSLMBs were galvanostaticly charged and discharged at a constant current of over 3–4.3 V at rates of 0.1 and 1 C at room temperature, while XCS and CT were performed alternately. For the cell (dis)charged at 0.1 C, XCS imaging was performed in the states of pristine (open circuit voltage, OCV), charging I (3.7 V), charging II (4.0 V), end of charge (4.3 V), discharging I (4.0 V), discharging II (3.7 V), and end of discharge (3.0 V), while CT was performed in the states of pristine, charging, end of charge, discharging, and end of discharge. For the SSLMB (dis)charged at 1 C, both XCS and CT were performed in the states of pristine, charging, end of charge, discharging, and end of discharge due to the shorter durations available for scanning during battery (dis)charging.

2.3. XCS-CT analysis

To perform correlative XCS-CT imaging, the CT data of the electrodes and the SPE membrane were superimposed onto the XCS imaging. Our previous study [40, 41] used XCS imaging to investigate the Li^+ chemical stoichiometry of the $LiNi_{0.8}Mn_{0.1}Co_{0.1}O_2$ (NMC811) cathode (~1 mm in thickness) made by directional ice templating [42–44]. In this study, we used a cathode and an SPE membrane of commercially standard thicknesses of ~65 and ~30 μm, respectively; their thicknesses were lower than the x-ray beam height (250 μm). This poses the challenge of separating scattering signals from the individual components. Here, we developed an analysis method to extract XCS signals from the individual components. The Li metal anode thickness was ~600 μm, and region 3 was for the Li metal anode only; hence, the Compton peak intensity was contributed by the Li metal anode only. The Compton peak intensity and the total electron density in the anode volume have a direct relationship [45], the intensity of the Compton peak of the SPE membrane I_s was calculated by

$$I_s = I_{R2} - \alpha \times I_{R3} \quad (2)$$

where I_{R2} and I_{R3} are the intensities of the Compton peaks in regions 2 and 3, respectively, and α is the vol% of the Li metal anode in region 2 w.r.t the anode volume in region 3. The intensity of the Compton peak of the cathode I_c was calculated by

$$I_c = I_{R1} - I_s - \beta \times I_{R3} \tag{3}$$

where I_{R1} is the intensity of the Compton peak in region 1 and β is the vol% of the Li metal anode in region 1 w.r.t the volume of the Li metal anode in region 3.

The Compton peak energy from the experimentally collected x-ray scattering energy spectra was validated by equation (4) [46], which shows the relationship between the incident x-ray wavelength λ and the inelastically scattered (Compton) x-ray wavelength λ' and converted to energy

$$\lambda' - \lambda = \frac{h}{mc}(1 - \cos\Theta) \tag{4}$$

where θ indicates the scattering angle, m is the mass of the electron, c is the speed of light, and h is Planck's constant. The electron momentum p_z was calculated according to equation (5) [46]:

$$\frac{p_z}{mc} \cong \frac{E_2 - E_1 + \left(\frac{E_2 E_1}{mc^2}\right)(1 - \cos\theta)}{\sqrt{E_1^2 + E_2^2 - 2E_1 E_2 \cos\theta}} \tag{5}$$

where E_1 is the incident x-ray energy while E_2 is the scattered x-ray energy. CT reconstruction was obtained by the method previously reported in [47–49].

The vol% of each component, α, was quantified and visualized in 3D using Avizo, MATLAB, and ImageJ [41, 50, 51]. We quantified the surface roughness in the horizontal or x–y plane through the arithmetic mean deviation, R_a, of the interphase between the anode and SPE membrane, and the buried interphase between the cathode and SPE membrane for the cells in the pristine, end of charge, and end of discharge states (dis)charged at different rates. A region of interest with a dimension of ~1300 × 160 × 1300 voxels (3.25 × 3.25 × 3.25 μm^3 per voxel) was extracted from the CT volume and reconstructed into 2D topology maps. Then, we used these 2D images to estimate R_a according to ISO4287:1997:

$$R_a = \frac{1}{A}\iint |Z(x,y)|\,dxdy \tag{6}$$

where $Z(x, y)$ indicates the ordinate across the area A along the horizontal plane. >6M data were used for each calculation.

3. Results and discussion

3.1. Electrochemical properties

Figure S1 shows the Nyquist plot of the SPE membrane between two electrodes of stainless steel at 25 °C, 50 °C, and 80 °C. The SPE ionic conductivity was estimated at 1.75 × 10^{-4} S cm^{-1} at 50 °C, corroborating the values reported in [52]. Figure 2(a) shows the galvanostatic charge and discharge curves of the full-cell SSLMB at 0.1 C of the first cycle and at 0.5 C of the second cycle, both tested at 60 °C. The charge and discharge capacities were 171 and 160 mAh g^{-1}, respectively, at 0.1 C, and 142 and 141 mAh g^{-1}, respectively, at 0.5 C. The reduced capacities at the higher C rate indicate more restricted Li^+ ion diffusion kinetics inside the SSLMB, and the discrepancy in capacities between charge and discharge indicates possible Li dendrite/irregular Li structure growth [44]. Figure S2 shows the cycling performance of the SSLMB, similar to other SSLMBs [53]. To analyze the oxidative stability, LSV was used in the SSLMB configuration; we changed the voltage and measured the current (figure 2(b)). A steady low current within changes of ~0.001 mA cm^{-2} was measured between 3.5 and 4.3 V due to Li^+ migration between the anode and cathode across the SPE [36]. As the voltage increased above 4.3 V, a current surge was observed and the rate of increase became significant at ⩾4.8 V, indicating an oxidation reaction at the cathode/SPE interphase; hence, a 3–4.3 V voltage window was selected for the (dis)charging profiles.

The EIS results of the SSLMB in the pristine, end of charge, and end of discharge states of the first cycle at 60 °C are shown in figure 2(c) (the high-to-medium frequency region is magnified in figure 2(d)). Both the real and imaginary impedance show that the impedance depends on the area of the samples, which is one of the main factors influencing interfacial ion transfer [54–56]. The intercept between the Nyquist plot and Z_{real} axis indicates the resistance of SPE; the first semicircle diameter at high-to-medium frequency indicates the interfacial resistance R_{int} between the electrodes and the SPE; and the second semicircle diameter at medium frequency indicates the charge transfer resistance R_{ct} of the electrodes [57]. R_{int} increased from 87.3 Ohm cm^2 at fully charged to 99.6 Ohm cm^2 at fully discharged, and R_{ct} also increased from fully charged to fully discharged, indicative of structural changes at the interphases [8], which will be investigated in detail below.

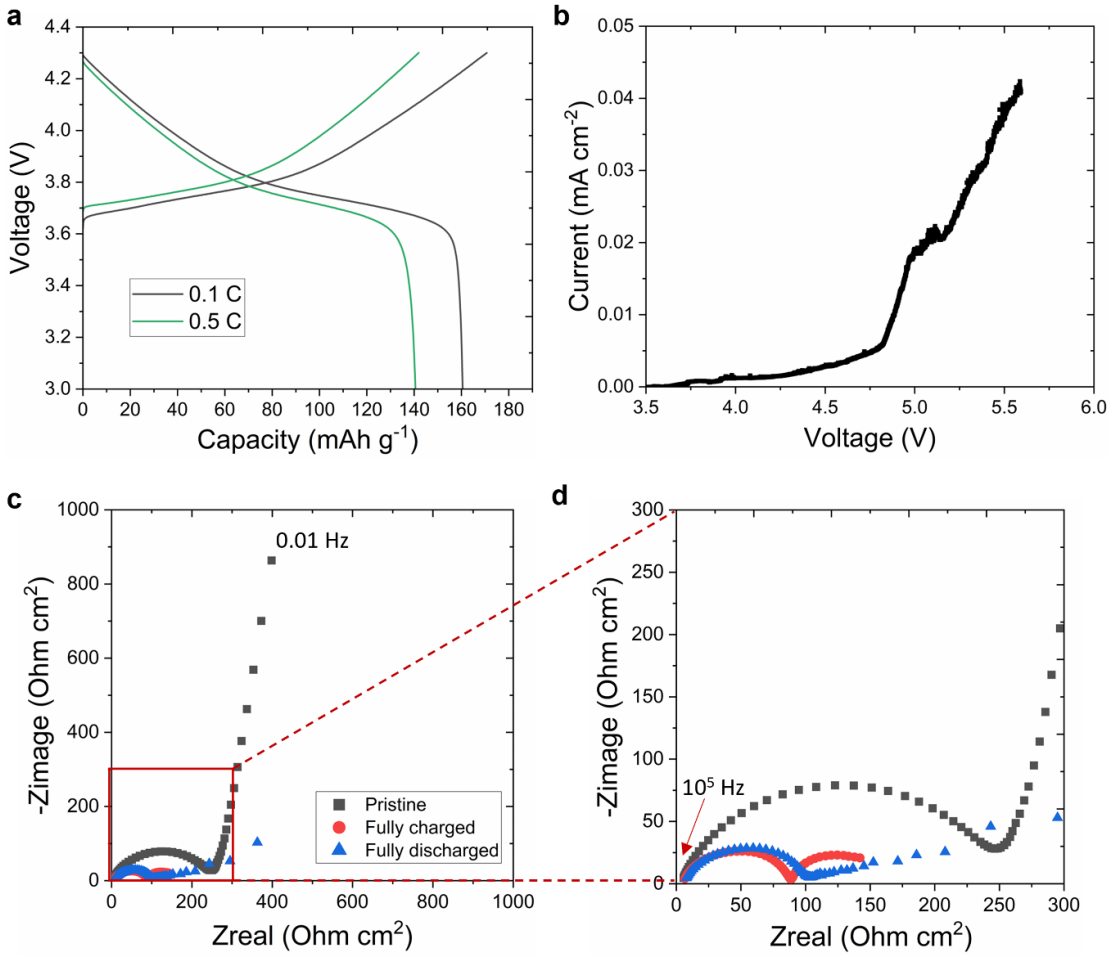

Figure 2. (a) *Ex situ* charge and discharge profiles at 0.1 and 0.5 C. (b) LSV graph of measured current as voltage increased. (c) Nyquist plot in the pristine, fully charged, and fully discharged states of the first cycle. (d) Magnified Nyquist plot in the high-to-medium frequency region.

3.2. Cathode characterization

To elucidate Li^+ concentration distributions in the cathode during (dis)charging, the XCS overall energy spectrum (the summed energy spectra of all pixels across the cathode plane) was analyzed. Previous studies showed that x-ray absorption at 115 keV was <1% [58, 59], the majority of the photons collected by the 2D spectroscopic detector were from the target plane of the battery [46], and the experimental setup controlled the angle of collection of the scattered photons, maximizing the accuracy of XCS analysis [60]. The x-ray energy spectra of the cathode inside an operating SSLMB in different (dis)charging states at a slow 0.1 C rate are shown in figure 3(a). The energy spectra of another cathode of the same composition and configuration under different (dis)charging states at a faster 1 C rate are shown in figure S3. The dominant 93.9 keV peak indicates the Compton peak, and was validated by equation (4), which shows the relationship between the incident x-ray wavelength and energy and the inelastically scattered photon wavelength and energy measured by the HEXITEC detector. The other small peaks at 22.9 and 26.1 keV and at 27.2 and 31.0 keV in both figures 3(a) and S3 are XRF signals of Cd and Te from the CdZnTe HEXITEC detector. The peaks at 50–85 keV are XRF signals from W and Pb due to the shielding and pinhole of the HEXITEC detector. The energy spectra in figures 3(a) and S3 show that the intensity differences among the Compton peaks in the different states are small because the peak intensity is related to the atomic scattering, which is related to the atomic electron density. The proportion of electron change (1 e^-) out of the total electrons of the NMC compound due to the Li^+ ion (de)intercalation is low (6.5% per NMC622 molecule) [45, 61]. This is one of the key reasons that most existing x-ray scattering methods do not have sufficient sensitivity toward the subtle changes of Li^+ concentrations in the cathode materials [62–67], and, hence, we develop the XCS method below.

Figure 3(b) shows the calculated Compton profiles that show the electron momentum p_z estimated from the Compton peak energy using equation 5. Figure 3(b) shows the Compton profile of the cathode in different (dis)charging states at 0.1 C (these states are used in order to compare with the same states

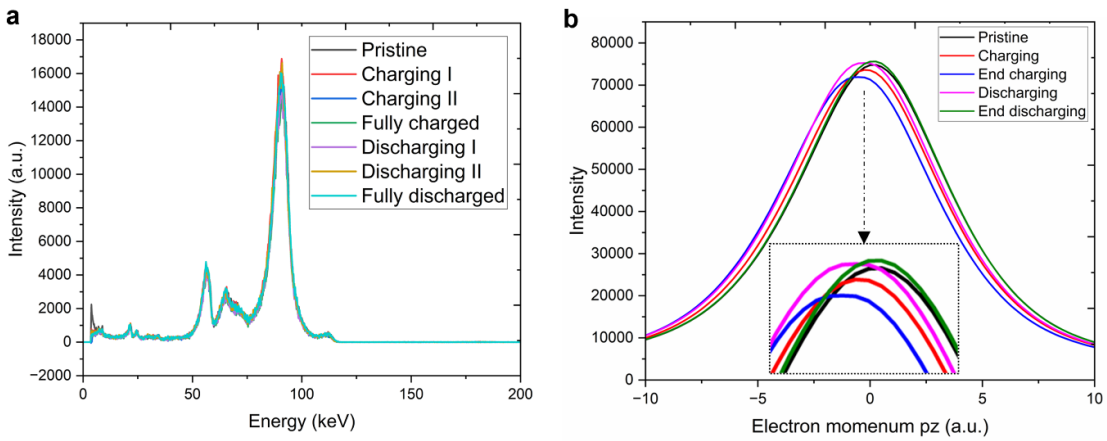

Figure 3. XCS results for the cathode inside operating SSLMB cells showing (a) x-ray scattering energy spectra; and (b) Compton profiles of the cathode; both under different (dis)charging states at 0.1 C. The peak intensities are the total spatial data points of spectra of all pixels along the cathode horizontal plane.

measured at 1 C). Figure S4 shows the corresponding calculated Compton profiles of the cathode at 1 C. The Compton profile analysis is able to distinguish between valence and core electrons of a compound because p_z is proportional to the orbital motion speed of electrons, v (i.e. the Compton profile shows the kinetics of electrons), and the orbital motion speed of the valence and core electrons is estimated to be $\sim 1.8 \times 10^6$ and 2.2×10^6 m s^{-1}, respectively [45]. This difference in orbital motion speed between the valence electron and core electron is larger than the difference in electron mass change above. We are particularly interested in the valence electrons since they are the ones being transferred between Li atoms and the cathode material electron orbital during (dis)charging redox reactions; hence, the Compton profile can distinguish the subtle Li^+ concentration evolution of the cathode material during (dis)charging. The intensities of the Compton profiles decreased from pristine to charging and to end charging, and increased from end charging to discharging and to end discharging, because Li^+ ions were removed from NMC622 during charging and intercalated back to NMC622 during discharging. In contrast, figure S4 shows the Compton profiles of the same cathode material under different states at 1 C, showing that the intensity trend was more random, and indicating that Li^+ ions were not sufficiently inserted into and removed from NMC622 at the faster C rate.

The electron momentum ratio (EMR) between the low electron momentum ($-1 < p_z < 1$) and high electron momentum ($-5 < p_z < -1$ and $1 < p_z < 5$) was calculated, where the low electron momentum refers to the valence electrons and the high electron momentum refers to the core electrons for the cathodes inside SSLMBs at 0.1 and 1 C. The p_z ranges of the valence and core electrons were estimated by measuring the XCS energy spectra of the cathode in the fully charged and discharged states [68], and were verified by measuring the Li concentration of the cathode compound material through inductively coupled plasma atomic emission spectroscopy [40, 41]. Figure S5 shows the linear relationship between the Li^+ chemical stoichiometry x in the $Li_xNi_{0.6}Mn_{0.2}Co_{0.2}O_2$ cathode and the EMR at different (dis)charging states at 0.1 C. Table 1 compares the calculated EMR and Li stoichiometry at the different states of the two cathodes (dis)charged at different rates, and shows that $Li_xNi_{0.6}Mn_{0.2}Co_{0.2}O_2$ was almost fully delithiated and lithiated during charging and discharging at 0.1 C, but much fewer Li^+ ions were removed from and inserted into $Li_xNi_{0.6}Mn_{0.2}Co_{0.2}O_2$ during delithiation and lithiation at 1 C. We quantified a 61% increase in the efficiency of extracting Li^+ ions from the NMC622 cathode to the anode during charging at 0.1 C compared with at 1 C, possibly due to the limited Li^+ ion diffusion inside SSLMB at the relatively faster rate, which hindered Li^+ migration at the cathode/SPE interphase and in the cathode [69].

Figure S6 compares the large field-of-view (8.5 mm × 8.5 mm along the horizontal plane) CT volume rendering at the interphase between SPE and cathode inside the SSLMBs at 0.1 and 1 C at the end of discharge. The cathode structure (dis)charged at 0.1 C (figure S6(a)) had a slightly higher roughness than that at 1 C (figure S6(b)), suggesting that more Li^+ ion movement resulted in a slight increase in interfacial roughness between the cathode and SPE.

3.3. Anode characterization

The Li metal anode was investigated by XCS-CT to reveal the corresponding relationship between the Li^+ ion concentration and microstructural changes at the anode/SPE interphase inside SSLMBs. Figure 4(a) compares the Compton profiles of the Li anode with the Compton profiles of the cathode in different (dis)charging states at 0.1 C (the top of the peaks of the anode is magnified in figure 4(b)). The intensities of

Table 1. Comparison of EMR and Li stoichiometry in $Li_xNi_{0.6}Mn_{0.2}Co_{0.2}O_2$ of cathodes inside SSLMBs at different (dis)charging states and rates.

	0.1 C		1 C	
State	EMR	Li stoichiometry of $Li_xNi_{0.6}Mn_{0.2}Co_{0.2}O_2$	EMR	Li stoichiometry of $Li_xNi_{0.6}Mn_{0.2}Co_{0.2}O_2$
Pristine (OCV)	1.21	1.01	1.20	1.01
Charging (3.7 V)	1.11	0.93	1.11	0.93
End of charge (4.3 V)	0.31	0.26	0.80	0.66
Discharging (3.7 V)	0.69	0.57	0.94	0.78
End of discharge (3 V)	1.09	0.91	1.09	0.91

the peaks are the sums of the data of all pixels along the horizontal plane of the anode. The intensities of the Compton profiles of the anode were all lower than those of the NMC622 cathode as the latter contained heavy transition metal elements of more electrons (∼47 electrons per molecule) and they scattered more photons than the light Li element (three electrons per atom) in the anode. The Compton profiles of the anode were also broader than those of the cathode. When the electrons are in motion, the Doppler effect relating to the electron velocities causes the Compton line to spread out [70]. The broader Compton profiles of the anode show that the kinetics of the valence electrons are more dominant in Li than in NMC622. Figure 4(b) shows the intensity of the Compton profiles of the anode increased gradually during charging (Li plating) and then decreased gradually during discharging (Li stripping). The Compton profiles of the cathode and anode inside the SSLMB under different (dis)charging states at 1 C (figure S7) show the same pattern that the peaks had lower intensities and were broader for the anode than the cathode. However, the intensity trend is more random under different (dis)charging states, again indicating a more limited Li^+ ion exchange at the faster rate, corroborating the cathode results in figure S4. Other than the intensity change, a slight peak shift can also be observed in the Compton profiles in figures 3(b), 4(a) and (b). This was likely caused by the inlet tubing of compressed air connected to the HEXITEC detector to keep the detector at a constant temperature of 18 °C during *operando* XCS imaging. The compressed air may have slightly affected the angle of the position of the detector, leading to a peak shift in the calculation of p_z in the Compton profiles (equation (5)). Future improvements of the experimental setup involve the use of a liquid cooling jacket outside the detector to minimize instability and movement of the detector.

The pixel-by-pixel XCS mapping of EMR in the horizontal plane for the cathode (figure 4(c)) and anode (figure 4(d)) under different (dis)charging states at 0.1 C shows that EMR generally increased at the anode/SPE interphase during charging (as Li^+ ions moved from the cathode, through SPE, to the anode during Li plating). EMR increased on the cathode during discharging (as Li^+ ions moved from the anode, through SPE, and back to the cathode during Li stripping). The mapping also shows laterally heterogeneous Li^+ transfer at both interphases.

Figure S8 shows a large field-of-view (8.5 × 8.5 mm^2 along the horizontal plane) CT 3D volume showing the anode/SPE interphase at the end of charge and discharge at 0.1 C. More irregular moss-like structures grew at the anode interphase than at the cathode interphase (figure S6), indicating a lower morphological stability for the Li metal anode than the cathode. The moss-like structures were more concentrated in the central part of the anode, correlating to the lateral heterogeneity of Li^+ ion concentrations from XCS imaging in figure 4(d).

Figure 5 shows the zoomed-in volume rendering of both the Li metal anode surface at the anode/SPE interphase and the bulk Li metal anode underneath at different (dis)charging states at 0.1 C inside the SSLMB. Individual Li dendrites started to grow during the plating of Li (figure 5(b)), and the Li dendrite growth direction was deflected, possibly due to the pressure exerted by the deformable SPE membrane at the anode interphase. However, surprisingly, during Li stripping, the heterogeneous Li structures at the interphase continued to grow, so there were more heterogeneous Li structures at the end of the stripping of Li than the plating. This is because pore formation took place in the underlying interfacial region (figure 5(d)), possibly due to the depletion of Li at the interphase [8]. The sub-surface pore/void volume continued to increase, and it is possible that some Li dendrites started to become isolated or form 'dead' Li (figure 5(e)) as some of the micropores were annihilated by plastic deformation [8]. Figure S9 shows the 3D volume rendering of another anode (with a similar volume of interest) in the same states at 1 C, showing that some irregular Li structures also grew at the anode/SPE interphase; however, the Li morphological changes were smaller at 1 C than at 0.1 C, possibly because only a few Li^+ ions were moved at the interphases within the limited (dis)charge duration at the higher C rate.

Table 2 summarizes the EMR and the quantification of surface roughness, R_a, at the anode and cathode interphases under different (dis)charging states at 0.1 and 1 C (example surface topological maps of the

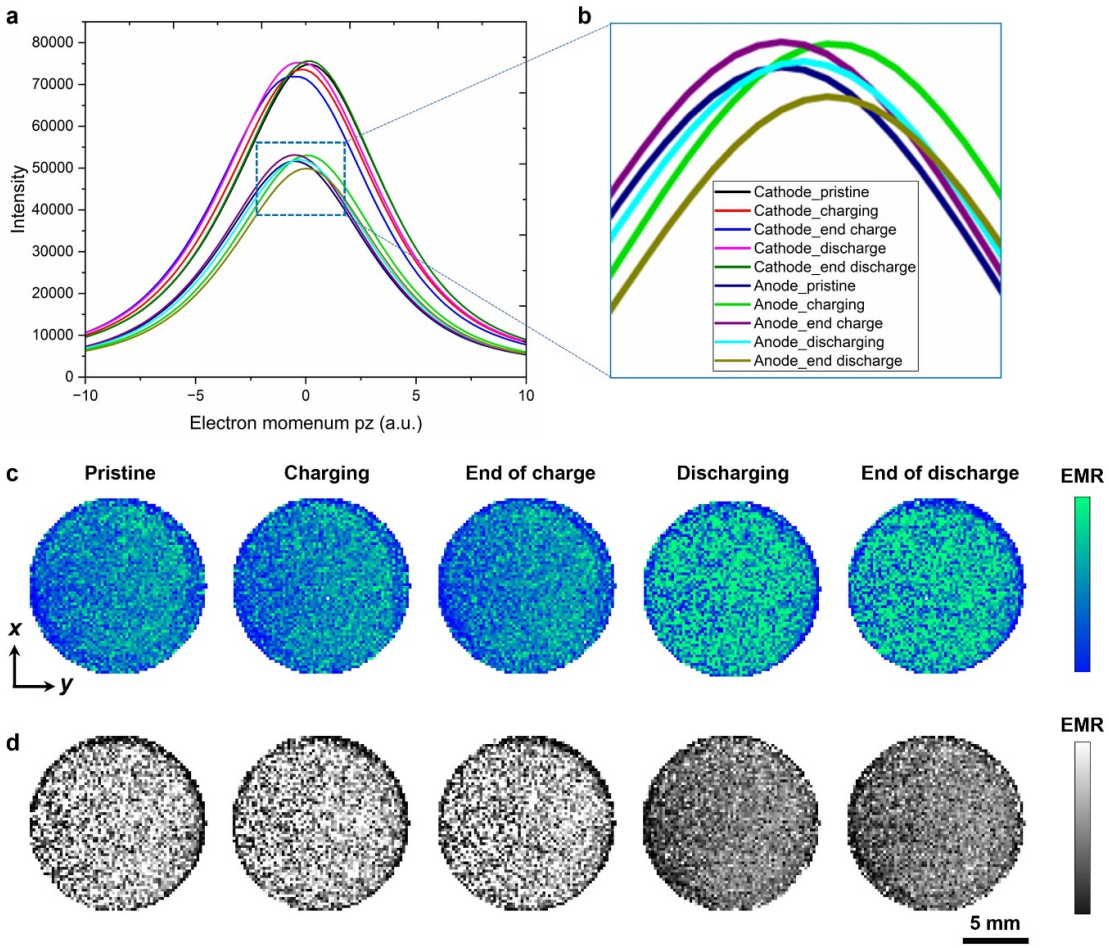

Figure 4. XCS imaging results for the anode and cathode inside operating SSLMB cells showing (a) Compton profiles (the intensities are the sums of data from all spatial pixels) along the horizontal plane of the Li metal anode and $Li_xNi_{0.6}Mn_{0.2}Co_{0.2}O_2$ cathode; (b) magnified top part of the peaks from (a); XCS mapping of EMR of (c) cathode and (d) anode along the horizontal plane, under the different (dis)charging states of pristine (OCV), charging (3.7 V), end of charge (4.3 V), discharging (3.7 V), and end of discharge (3 V), at 0.1 C.

anode at the anode/SPE interphase under charged state at 0.1 and 1 C are shown in figure S10). Table 2 quantifies and shows that R_a increased from the pristine state to the end of charge, and continued to increase from the end of charge to the end of discharge for both the cathode and anode at both rates, with a higher increase rate of R_a for the anode compared with the cathode, and a higher increase rate during Li stripping compared with plating, e.g. R_a at the anode side increased by 13.4% during Li stripping compared with 6.1% during Li plating at 0.1 C during the first cycle. This shows that more irregular Li structure growth was accelerated during the Li stripping step instead of during the Li plating step, in agreement with the higher R_{int} and R_{ct} during Li stripping measured by EIS in figure 2. This phenomenon may be due to two reasons: the first is the onset of imbalance of Li^+ ion diffusion between the two electrodes (the Li^+ concentration change rate between charging and discharging more than doubled for the cathode compared with the anode as shown by the EMR, particularly at 0.1 C), i.e. the extent of the reduction reaction at the cathode side exceeds that of the oxidation side reaction at the anode side during discharging. The second reason is that Li^+ ions were stripped from a porous morphology (developed during the first plating) and resulted in a more non-uniform surface with irregular Li^0 structures.

Possible strategies to reduce the irregular Li structures at the interphase between the anode and SPE include using asymmetric (dis)charging protocols of different current densities during charging and discharging [33], and using a high current discharging for 1–2 min to induce isolated 'dead' Li to dissolve on one end and re-deposit on the other end to re-connect to the anode [34] after every few cycles, so that the following Li stripping cycle takes place on a less heterogeneous surface.

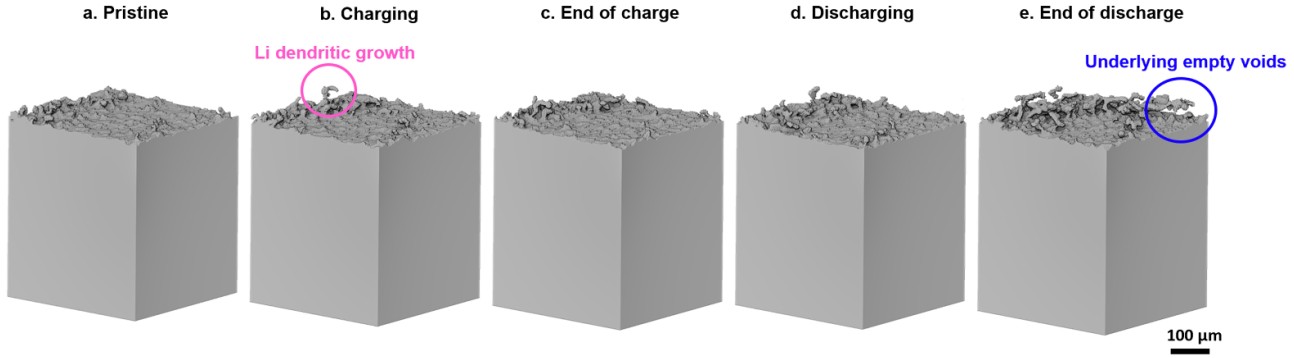

Figure 5. 3D visualization of the Li anode inside an operating full-cell SSLMB. The 3D volume rendering shows changes of anode surface (at the buried interphase between anode and SPE membrane) and bulk anode volume at (a) pristine (OCV), (b) charging (4 V), (c) end of charge (4.3 V), (d) discharging (4 V), and (e) end of discharge (3 V), at 0.1 C.

Table 2. EMR and surface roughness R_a in the horizontal plane of the cathode/SPE and anode/SPE interphases inside SSLMBs at different (dis)charging states and at different rates.

	0.1 C				1 C			
	Anode/SPE interphase		Cathode/SPE interphase		Anode/SPE interphase		Cathode/SPE interphase	
State	EMR	R_a (μm)	EMR	R_a (μm)	EMR	R_a (μm)	EMR	R_a (μm)
Pristine (OCV)	1.28	5.07	1.21	2.12	1.28	3.58	1.20	2.11
Charging (3.7 V)	1.36	5.28	1.11	2.21	1.32	3.87	1.11	2.15
End of charge (4.3 V)	1.73	5.38	0.31	2.25	1.33	3.99	0.80	2.21
Discharging (3.7 V)	1.51	5.73	0.69	2.43	1.32	4.01	0.94	2.26
End of discharge (3 V)	1.41	6.10	1.09	2.49	1.25	4.06	1.09	2.27

4. Conclusion

The interplay between Li^+ ion diffusion and Li^0 metal structure evolution at the buried interphases on both the anode and cathode sides inside SSLMBs in commercially standard coin cell configurations was directly imaged *in operando* using a novel correlative XCS-CT imaging technique for the first time. We emphasize that studying Li^+ ion concentrations and Li^0 morphology simultaneously inside a full cell is challenging, particularly because of the low signal-to-noise ratio of the ultra-light Li element, and we look at the development of the new *operando* correlative XCS-CT imaging method to study the valence electron momentum and hence the chemical properties of the materials in correlation with physical structural changes. The results showed that the efficiency of extracting Li^+ ions from the cathode NMC622 material during charging was 61% higher at 0.1 C than at 1 C. The roughness R_a at both the cathode and anode interphases was quantified at different (dis)charging states and rates. R_a increased during Li plating and continued to increase during Li stripping, with $R_a = 1.7–2.5$ times higher at the anode interphase than at the cathode interphase under the various (dis)charge states at 0.1 and 1 C. The irregular Li structure growth with sub-surface pore formation was accelerated during the Li stripping step, leading to Li^+ deficiency at the anode interphase, loss of homogeneous contact at the anode/SPE interphase, and increased interfacial and charge transfer resistance. The initiation and growth mechanisms of the irregular Li structures at the anode/SPE interphase were due to the onset of Li^+ ion diffusion imbalance between the cathode and anode. Overall, the mechanism examined here provides a foundation for understanding the root cause of the irregular Li structures and potential solutions for mitigating the excessive Li structure irregularity inside SSLMBs.

Data availability statement

All data that support the findings of this study are included within the article (and any supplementary files).

Acknowledgment

The XCS-CT experiment (beamtime proposal MG29851) was conducted at the beamline I12-JEEP (Joint Engineering, Environmental and Processing), Diamond Light Source, UK. CH is grateful for the funding from the Faraday Institution Battery Degradation programme (FIRG060, FIRG082) and Nextrode programme (FIRG066), Industry Fellowship (FIIF015), and Training Grant (FITG034). CH also acknowledges the ERC Starting Grant (UKRI Guarantee Fund EP/Y009908/1), Imperial College London UKRI Impact Acceleration Account (EP/X52556X/1), and the EPSRC Innovation Fellowship (EP/S001239/1, EP/S001239/2). CLAL is grateful for the UKRI EPSRC funding of projects: 'Data-driven, Reliable, and Effective Additive Manufacturing using multi-BEAM technologies' (EP/W037483/1), 'Future Manufacturing Hub' (EP/P006566/1), 'Made Smarter Innovation—Materials Made Smarter Research Centre' (EP/V061798/1), 'Performance-driven design of aluminium alloys for additive manufacturing' (EP/W006774/1), 'Manufacturing by Design' (EP/W003333/1), and IPG Photonics/Royal Academy of Engineering Senior Research Fellow in Synchrotron calibratEd lAser pRocessing teCHnologies (SEARCH) (ref: RCSRF2324-18-71). We also thank Dr Enzo Liotti, Professor Steve Collins, and Dr Oxana Magdysyuk for their participation in the experiment MG29851.

Conflict of interest

There are no conflicts to declare.

ORCID iDs

Chun Huang https://orcid.org/0000-0001-6548-2977
Abeiram Sivarajah https://orcid.org/0009-0005-2330-6138
Wiebe Stolp https://orcid.org/0000-0003-0282-4401
Thomas Connolley https://orcid.org/0000-0002-1851-3467
Chu Lun Alex Leung https://orcid.org/0000-0002-4153-7512

References

[1] Genreith-Schriever A R, Alexiu A, Phillips G S, Coates C S, Nagle-Cocco L A, Bocarsly J D, Sayed F N, Dutton S E and Grey C P 2024 Jahn–teller distortions and phase transitions in $LiNiO_2$: insights from Ab initio molecular dynamics and variable-temperature x-ray diffraction *Chem. Mater.* **36** 2289–303

[2] Cuesta A F, Dickson S A, Naden A B, Lonsdale C and Irvine J T 2023 Influence of electrode processing and electrolyte composition on multiwall carbon nanotube negative electrodes for sodium ion batteries *J. Phys. Energy* **5** 015004
[3] Koo B-R, Lee Y-G, Lee S H, An G-H and Huang C 2022 One-pot spray engineering to design $Na_{0.44}MnO_2$ cathode electrodes for high-rate and cycle-stable Na-Ion batteries *Batteries* **8** 181
[4] Xu W, Wang J, Ding F, Chen X, Nasybulin E, Zhang Y and Zhang J-G 2014 Lithium metal anodes for rechargeable batteries *Energy Environ. Sci.* **7** 513–37
[5] Lin D, Liu Y and Cui Y 2017 Reviving the lithium metal anode for high-energy batteries *Nat. Nanotechnol.* **12** 194
[6] Famprikis T, Canepa P, Dawson J A, Islam M S and Masquelier C 2019 Fundamentals of inorganic solid-state electrolytes for batteries *Nat. Mater.* **18** 1278–91
[7] Liu S, Liu W, Ba D, Zhao Y, Ye Y, Li Y and Liu J 2023 Filler-integrated composite polymer electrolyte for solid-state lithium batteries *Adv. Mater.* **35** 2110423
[8] Krauskopf T, Mogwitz B, Rosenbach C, Zeier W G and Janek J 2019 Diffusion limitation of lithium metal and Li–Mg alloy anodes on LLZO type solid electrolytes as a function of temperature and pressure *Adv. Energy Mater.* **9** 1902568
[9] Kasemchainan J, Zekoll S, Spencer Jolly D, Ning Z, Hartley G O, Marrow J and Bruce P G 2019 Critical stripping current leads to dendrite formation on plating in lithium anode solid electrolyte cells *Nat. Mater.* **18** 1105–11
[10] Björklund E, Xu C, Dose W M, Sole C G, Thakur P K, Lee T-L, De Volder M F, Grey C P and Weatherup R S 2022 Cycle-induced interfacial degradation and transition-metal cross-over in $LiNi_{0.8}Mn_{0.1}Co_{0.1}O_2$–graphite cells *Chem. Mater.* **34** 2034–48
[11] Dose W M, Xu C, Grey C P and De Volder M F 2020 Effect of anode slippage on cathode cutoff potential and degradation mechanisms in Ni-rich Li-ion batteries *Cell Rep. Phys. Sci.* **1** 100253
[12] Zhao Z, Zhang X, Wang P, Pateli I M, Gao H, Wang G and Irvine J T 2024 New approaches to three-dimensional positive electrodes enabling scalable high areal capacity *J. Mater. Chem.* A **12** 1736–45
[13] Björklund E, Brandell D, Hahlin M, Edström K and Younesi R 2017 How the negative electrode influences interfacial and electrochemical properties of $LiNi_{1/3}Co_{1/3}Mn_{1/3}O_2$ cathodes in Li-ion batteries *J. Electrochem. Soc.* **164** A3054
[14] McConohy G, Xu X, Cui T, Barks E, Wang S, Kaeli E, Melamed C, Gu X W and Chueh W C 2023 Mechanical regulation of lithium intrusion probability in garnet solid electrolytes *Nat. Energy* **8** 241–50
[15] Merryweather A J, Schnedermann C, Jacquet Q, Grey C P and Rao A 2021 Operando optical tracking of single-particle ion dynamics in batteries *Nature* **594** 522–8
[16] Merryweather A J, Jacquet Q, Emge S P, Schnedermann C, Rao A and Grey C P 2022 Operando monitoring of single-particle kinetic state-of-charge heterogeneities and cracking in high-rate Li-ion anodes *Nat. Mater.* **21** 1306–13
[17] He Y, Ren X, Xu Y, Engelhard M H, Li X, Xiao J, Liu J, Zhang J-G, Xu W and Wang C 2019 Origin of lithium whisker formation and growth under stress *Nat. Nanotechnol.* **14** 1042–7
[18] Gonzalez-Rosillo J C, Guc M, Liedke M O, Butterling M, Attallah A G, Hirschmann E, Wagner A, Izquierdo-Roca V, Baiutti F and Morata A 2024 Insights into the $LiMn_2O_4$ cathode stability in aqueous electrolytes *Chem. Mater.* **36** 6144–53
[19] Lu X, Schreiber D K, Neeway J J, Ryan J V and Du J 2017 Effects of optical dopants and laser wavelength on atom probe tomography analyses of borosilicate glasses *J. Am. Ceram. Soc.* **100** 4801–15
[20] Ning Z, Jolly D S, Li G, De Meyere R, Pu S D, Chen Y, Kasemchainan J, Ihli J, Gong C and Liu B 2021 Visualizing plating-induced cracking in lithium-anode solid-electrolyte cells *Nat. Mater.* **20** 1121–9
[21] Ning Z, Li G, Melvin D L, Chen Y, Bu J, Spencer-Jolly D, Liu J, Hu B, Gao X and Perera J 2023 Dendrite initiation and propagation in lithium metal solid-state batteries *Nature* **618** 287–93
[22] Pfaff J, Fransson M, Broche L, Buckwell M, Finegan D P, Moser S, Schopferer S, Nau S, Shearing P R and Rack A 2023 *In situ* chamber for studying battery failure using high-speed synchrotron radiography *J. Synchrotron Radiat.* **30** 192–9
[23] Han F, Westover A S, Yue J, Fan X, Wang F, Chi M, Leonard D N, Dudney N J, Wang H and Wang C 2019 High electronic conductivity as the origin of lithium dendrite formation within solid electrolytes *Nat. Energy* **4** 187–96
[24] Sha Z, Kerherve G, van Spronsen M A, Wilson G E, Kilner J A, Held G and Skinner S J 2023 Studying surface chemistry of mixed conducting perovskite oxide electrodes with synchrotron-based soft x-rays *J. Phys. Chem.* C **127** 20325–36
[25] Dawkins J I, Martens I, Danis A, Beaulieu I, Chhin D, Mirolo M, Drnec J, Schougaard S B and Mauzeroll J 2023 Mapping the total lithium inventory of Li-ion batteries *Joule* **7** 2783–97
[26] Chen R, Leung C L A and Huang C 2024 Exploring the properties of disordered rocksalt battery cathode materials by advanced characterization *Adv. Funct. Mater.* **34** 2308165
[27] Ren Y and Zuo X 2018 Synchrotron X-ray and neutron diffraction, total scattering, and small-angle scattering techniques for rechargeable battery research *Small Methods* **2** 1800064
[28] Liu T, Leskes M, Yu W, Moore A J, Zhou L, Bayley P M, Kim G and Grey C P 2015 Cycling Li-O_2 batteries via LiOH formation and decomposition *Science* **350** 530–3
[29] Liu H, Strobridge F C, Borkiewicz O J, Wiaderek K M, Chapman K W, Chupas P J and Grey C P 2014 Capturing metastable structures during high-rate cycling of $LiFePO_4$ nanoparticle electrodes *Science* **344** 1252817
[30] Pecher O, Carretero-González J, Griffith K J and Grey C P 2017 Materials' methods: NMR in battery research *Chem. Mater.* **29** 213–42
[31] Gao Y, Yan Z, Gray J L, He X, Wang D, Chen T, Huang Q, Li Y C, Wang H and Kim S H 2019 Polymer–inorganic solid–electrolyte interphase for stable lithium metal batteries under lean electrolyte conditions *Nat. Mater.* **18** 384–9
[32] Chen Z, Jia H, Yan S and Gohy J-F 2023 Polymer-coated silica dual functional fillers to improve the performance of poly (ethylene oxide)-based solid electrolytes *Nano Energy* **114** 108637
[33] Louli A, Coon M, Genovese M, Degooyer J, Eldesoky A and Dahn J 2021 Optimizing cycling conditions for anode-free lithium metal cells *J. Electrochem. Soc.* **168** 020515
[34] Liu F, Xu R, Wu Y, Boyle D T, Yang A, Xu J, Zhu Y, Ye Y, Yu Z and Zhang Z 2021 Dynamic spatial progression of isolated lithium during battery operations *Nature* **600** 659–63
[35] Biancolli A L G, Konovalova A, Santiago E I and Holdcroft S 2023 Measuring the ionic conductivity of solid polymer electrolyte powders *Int. J. Electrochem. Sci.* **18** 100288
[36] Xiong Z, Wang Z, Zhou W, Liu Q, Wu J-F, Liu T-H, Xu C and Liu J 2023 4.2 V polymer all-solid-state lithium batteries enabled by high-concentration PEO solid electrolytes *Energy Storage Mater.* **57** 171–9
[37] Lu J, Zhou J, Chen R, Fang F, Nie K, Qi W, Zhang J-N, Yang R, Yu X and Li H 2020 4.2 V poly (ethylene oxide)-based all-solid-state lithium batteries with superior cycle and safety performance *Energy Storage Mater.* **32** 191–8
[38] Veale M C, Booker P, Cross S, Hart M D, Jowitt L, Lipp J, Schneider A, Seller P, Wheater R M and Wilson M D 2020 Characterization of the uniformity of high-flux CdZnTe material *Sensors* **20** 2747

[39] Van Assche F, Vanheule S, Van Hoorebeke L and Boone M N 2021 The spectral x-ray imaging data acquisition (spexidaq) framework *Sensors* **21** 563

[40] Huang C, Wilson M D, Suzuki K, Liotti E, Connolley T, Magdysyuk O V, Collins S, Van Assche F, Boone M N and Veale M C 2022 3D correlative imaging of lithium ion concentration in a vertically oriented electrode microstructure with a density gradient *Adv. Sci.* **9** 2105723

[41] Leung C L A *et al* 2023 Correlative full field x-ray compton scattering imaging and x-ray computed tomography for *in situ* observation of Li ion batteries *Mater. Today Energy* **31** 101224

[42] Huang C and Grant P S 2018 Coral-like directional porosity lithium ion battery cathodes by ice templating *J. Mater. Chem.* A **6** 14689–99

[43] Huang C, Dontigny M, Zaghib K and Grant P S 2019 Low-tortuosity and graded lithium ion battery cathodes by ice templating *J. Mater. Chem.* A **7** 21421–31

[44] Huang C, Leung C L A, Leung P and Grant P S 2020 A solid-state battery cathode with a polymer composite electrolyte and low tortuosity microstructure by directional freezing and polymerization *Adv. Energy Mater.* **11** 2002387

[45] Suzuki K, Barbiellini B, Orikasa Y, Kaprzyk S, Itou M, Yamamoto K, Wang Y J, Hafiz H, Uchimoto Y and Bansil A 2016 Non-destructive measurement of in-operando lithium concentration in batteries via x-ray Compton scattering *J. Appl. Phys.* **119** 025103

[46] Itou M, Orikasa Y, Gogyo Y, Suzuki K, Sakurai H, Uchimoto Y and Sakurai Y 2015 Compton scattering imaging of a working battery using synchrotron high-energy x-rays *J. Synchrotron Radiat.* **22** 161–4

[47] Atwood R C, Bodey A J, Price S W, Basham M and Drakopoulos M 2015 A high-throughput system for high-quality tomographic reconstruction of large datasets at diamond light source *Phil. Trans. R. Soc.* A **373** 20140398

[48] Vo N T, Atwood R C and Drakopoulos M 2018 Superior techniques for eliminating ring artifacts in x-ray micro-tomography *Opt. Express* **26** 28396–412

[49] Wadeson N and Basham M 2016 Savu: a Python-based, MPI framework for simultaneous processing of multiple, N-dimensional, large tomography datasets (arXiv:1610.08015)

[50] Huang C, Wilson M D, Cline B, Sivarajah A, Stolp W, Boone M N, Connolley T and Leung C L A 2024 Correlating lithium-ion transport and interfacial lithium microstructure evolution in solid-state batteries during the first cycle *Cell Rep. Phys. Sci.* **5** 101995

[51] Leung C L A, Wilson M D, Connolley T and Huang C 2024 Mapping of lithium ion concentrations in 3D structures through development of *in situ* correlative imaging of X-ray Compton scattering-computed tomography *J. Synchrotron Radiat.* **31** 888–95

[52] Kaboli S, Demers H, Paolella A, Darwiche A, Dontigny M, Clément D, Guerfi A, Trudeau M L, Goodenough J B and Zaghib K 2020 Behavior of solid electrolyte in Li-Polymer battery with NMC cathode via *in-situ* scanning electron microscopy *Nano Lett.* **20** 1607–13

[53] Kim J-S, Yoon G, Kim S, Sugata S, Yashiro N, Suzuki S, Lee M-J, Kim R, Badding M and Song Z 2023 Surface engineering of inorganic solid-state electrolytes via interlayers strategy for developing long-cycling quasi-all-solid-state lithium batteries *Nat. Commun.* **14** 782

[54] Okafor P A and Iroh J O 2015 Fabrication of porous graphene/polyimide composites using leachable poly-acrylic resin for enhanced electrochemical and energy storage capabilities *J. Mater. Chem.* A **3** 17230–40

[55] Thompson R S, Schroeder D J, López C M, Neuhold S and Vaughey J T 2011 Stabilization of lithium metal anodes using silane-based coatings *Electrochem. Commun.* **13** 1369–72

[56] Gordon I J, Grugeon S, Takenouti H, Tribollet B, Armand M, Davoisne C, Débart A and Laruelle S 2017 Electrochemical impedance spectroscopy response study of a commercial graphite-based negative electrode for Li-ion batteries as function of the cell state of charge and ageing *Electrochim. Acta* **223** 63–73

[57] Herbers L, Minář J, Stuckenberg S, Küpers V, Berghus D, Nowak S, Winter M and Bieker P 2023 The influence of polyethylene oxide degradation in polymer-based electrolytes for NMC and lithium metal batteries *Adv. Energy Sustain. Res.* **4** 2300153

[58] Brancewicz M, Itou M and Sakurai Y 2016 A Monte Carlo study of high-energy photon transport in matter: application for multiple scattering investigation in Compton spectroscopy *J. Synchrotron Radiat.* **23** 244–52

[59] Bugby S, Koch-Mehrin K, Veale M, Wilson M and Lees J 2019 Energy-loss correction in charge sharing events for improved performance of pixellated compound semiconductors *Nucl. Instrum. Methods Phys. Res.* A **940** 142–51

[60] Xiao R, Sato S, Uyama C and Nakamura T 1994 Fundamental study of Compton scattering tomography

[61] Cooper M, Cooper M J, Mijnarends P, Mijnarends P E, Shiotani N, Sakai N and Bansil A 2004 *x-ray Compton Scattering* (Oxford University Press on Demand)

[62] Friedrich F, Strehle B, Freiberg A T, Kleiner K, Day S J, Erk C, Piana M and Gasteiger H A 2019 Capacity fading mechanisms of NCM-811 cathodes in lithium-ion batteries studied by x-ray diffraction and other diagnostics *J. Electrochem. Soc.* **166** A3760

[63] Heenan T M, Wade A, Tan C, Parker J E, Matras D, Leach A S, Robinson J B, Llewellyn A, Dimitrijevic A and Jervis R 2020 Identifying the origins of microstructural defects such as cracking within Ni-rich NMC811 cathode particles for lithium-ion batteries *Adv. Energy Mater.* **10** 2002655

[64] Vamvakeros A, Matras D, Ashton T E, Coelho A A, Dong H, Bauer D, Odarchenko Y, Price S W, Butler K T and Gutowski O 2021 Cycling rate-induced spatially-resolved heterogeneities in commercial cylindrical Li-Ion batteries *Small Methods* **5** 2100512

[65] Daemi S R, Tan C, Vamvakeros A, Heenan T M, Finegan D P, Di Michiel M, Beale A M, Cookson J, Petrucco E and Weaving J S 2020 Exploring cycling induced crystallographic change in NMC with x-ray diffraction computed tomography *Phys. Chem. Chem. Phys.* **22** 17814–23

[66] Heenan T, Mombrini I, Llewellyn A, Checchia S, Tan C, Johnson M, Jnawali A, Garbarino G, Jervis R and Brett D 2023 Mapping internal temperatures during high-rate battery applications *Nature* **617** 507–12

[67] Egami T and Billinge S J 2003 *Underneath the Bragg Peaks: Structural Analysis of Complex Materials* (Elsevier)

[68] Suzuki K, Kanai R, Tsuji N, Yamashige H, Orikasa Y, Uchimoto Y, Sakurai Y and Sakurai H 2018 Dependency of the charge–discharge rate on lithium reaction distributions for a commercial lithium coin cell visualized by Compton scattering imaging *Condens. Matter* **3** 27

[69] Usubelli C, Besli M M, Kuppan S, Jiang N, Metzger M, Dinia A, Christensen J and Gorlin Y 2020 Understanding the overlithiation properties of $LiNi_{0.6}Mn_{0.2}Co_{0.2}O_2$ using electrochemistry and depth-resolved x-ray absorption spectroscopy *J. Electrochem. Soc.* **167** 080514

[70] Rao D, Cesareo R, Brunetti A, Gigante G E, Akatsuka T, Takeda T and Itai Y 2004 Doppler broadening calculations of Compton scattering for molecules, plastics, tissues, and few biological materials in the x-ray region: an analysis in terms of Compton broadening and geometrical energy broadening *J. Phys. Chem. Ref. Data* **33** 627–712